Dynamic Nanoindentation and Short-Range Order in Equiatomic NiCoCr Medium-Entropy Alloy Lead to Novel Density Wave Ordering

A. Naghdi,[1,2] F. J. Domínguez-Gutiérrez,[1] W. Y. Huo,[1,3] K. Karimi,[1] and S. Papanikolaou[1,*]
[1]NOMATEN Centre of Excellence, National Center for Nuclear Research, ulica A. Sołtana 7, 05-400 Swierk/Otwock, Poland
[2]IDEAS NCBR, ulica Chmielna 69, 00-801 Warsaw, Poland
[3]College of Mechanical and Electrical Engineering, Nanjing Forestry University, Nanjing 210037, China

(Received 10 November 2022; revised 27 December 2023; accepted 9 February 2024; published 12 March 2024)

Chemical short-range order is believed to be a key contributor to the exceptional properties of multicomponent alloys. However, its direct validation and confirmation has been highly elusive in most compounds. Recent studies for equiatomic NiCoCr alloys have shown that thermal treatments (i.e., annealing and aging) may facilitate and manipulate such ordering. In this work, by using molecular simulations, we show that nanomechanical probes, such as nanoindentation, may be utilized toward further manipulation of chemical short-range order, providing explicit validation pathways. By using well established interatomic potentials, we perform hybrid molecular-dynamics–Monte Carlo at room temperature to demonstrate that particular dwell nanoindentation protocols can lead, through thermal Monte Carlo equilibration, to local reorganization under the indenter tip, toward a density-wave stripe pattern. We characterize the novel density-wave structures, which are highly anisotropic and dependent on local, nanoindentation-induced stress concentrations, and we show how they deeply originate from intrinsic features of interelemental interactions. Furthermore, we show that these novel patterns consistently scale with the incipient plastic zone, under the indenter tip, justifying their observation at experimentally feasible nanoindentation depths.

DOI: 10.1103/PhysRevLett.132.116101

Concentrated multicomponent alloys, and in particular, the celebrated Cantor alloys [1–3], such as equiatomic single-phase CoCrFeMnNi, have been instrumental into guiding the exploration for the discovery of affordable, durable alloys, suitable for applications under extreme conditions [4,5]. It has been conjectured that a major contributor to the exceptional properties of these alloys is the formation of chemical short-range (1 nm) order (CSRO) that may pin or/and obstruct moving lattice defects, such as dislocations. While the observation of CSRO is quite common in such complex alloys, its causal connection to *exceptional* mechanical properties has been a subject of intense debate. Extensive investigations have culminated toward the focus shining on the curious case of single-phase equiatomic NiCoCr. This alloy has outstanding mechanical properties, namely hardness, strength, and ductility [6], and there is plausible formation of CSROs in the alloys, especially after sample aging at high temperatures [7–11]. Numerous studies have explored the nanoindentation creep behavior of materials such as high-entropy alloys, nanoglass films, and medium-entropy alloys demonstrating that factors such as internal structure, external loading sequence, and strain rate sensitivity significantly influence creep behavior, where thermomechanical processing can improve performance under shock loads [12–16]. On one hand, it has been observed that dislocation stacking fault widths are sensitive to the formation of such short-range order [14,17], which is commonly (in metallurgy) associated with large(r) mechanical strength.

Moreover, such improvements in NiCoCr strength have been also greatly attributed to solid solution strengthening, due to lattice distortion effects, with no or very little contributions from short-range ordering [18]. Therefore, a deeper understanding of CSRO is required to identify how to control and possibly, augment CSRO features, and check its causal effects on mechanical properties. For this purpose, in this work, we theoretically consider dwell nanoindentation as a possible way to locally manipulate CSRO in equiatomic NiCoCr, and lead to causal connections between hardness and microscopy-resolvable nanostructural features. We utilize molecular simulation, as well as Monte Carlo methods, and we show that CSRO (if it exists) will be unstable to the formation of unconventional density-wave ordered (DWO) stripe patterns, that are highly anisotropic and originate due to interatomic potential features.

CSRO is commonly observable at the nanoscale, ranging between 0.5–2 nm in linear size [8]. Starting from a random

solid solution (RSS), it is natural to expect that constituent element enthalpic interactions may cause CSRO formation at the atomic scale [7,11,14,18–29]. CSROs have a notable effect on defects (dislocations, interstitials, and vacancies, etc.) and their dynamical behavior, as well as macroscopic alloy mechanical properties [7,14,18,19,27–30]. CSRO is commonly inferred through implicit experimental measurements, through their relation to macroscopic properties, such as stacking-fault energy, hardness, irradiation effects, etc. [24–26,31]. CSRO is also investigated in theoretical and computational works [10,27,32], with the most intense focus being on the case of equiatomic NiCoCr [17,27]. Molecular dynamics (MD), spin polarized density functional theory [10], but also Monte Carlo (MC) simulations have been utilized to characterize CSRO structural features [32].

Creep deformation studies in multicomponent alloys are abundant [33–39]. Here, we aim at utilizing creep deformation to comprehend in a deeper sense the character of CSRO by promoting nontrivial predictions for elemental density wave ordering at the nanoscale. While uniaxial testing [39–43] and nanoindentation, alongside microscopy, have been used for the elucidation of lattice defect deformation mechanisms [44], the constant-load dwell nanoindentation tests, between 1 min to 10 h of dwell time, have been solely popular for investigating the relation between hardness and indentation strain rate over a, possibly wide, temperature range [45–48]. We use this concept to generate predictions for CSRO nanopatterning at room temperature that may be directly observable using electron microscopy techniques. While this work is fully focused on modeling aspects and predictions for CSRO saturation regimes that may emerge at each loading depth, prior alloy studies [45–48] shall allow us to conclude that the proposed scenario is attainable at room conditions.

In this Letter, we utilize hybrid MC-MD simulations, using LAMMPS [49], to demonstrate the plausible thermomechanical effects of a dwell nanoindentation scenario in single-phase equiatomic RSS NiCoCr. RSS samples were generated using random elemental sampling on appropriate face-centered cubic (FCC) lattices, with crystal orientations of $x = [100]$, $y = [010]$, and $z = [001]$ or $x = [100]$, $y = [01\bar{1}]$, and $z = [011]$, and dimensions $25.85 \times 23.59 \times 15.14$ nm^3. Samples then undergo energy minimization at $T = 0$ K and then relaxation for 100 ps at $T = 300$ K with time discretization $\Delta t \simeq 1.0$ fs, in an isothermal–isobaric (NPT) ensemble at temperature T, pressure P and particle number N, with a Nose-Hoover thermostat and barostat with relaxation time scales of $\tau_d^{\text{therm}} = 10$ fs and $\tau_d^{\text{bar}} = 100$ fs, using an embedded-atom method-based potential, first proposed by Li *et al.* [27], who also showed that annealing of the samples (even at room temperature) leads to the formation of characteristic Ni-rich SRO patterning, which we will generally refer to as short-range order (SRO) samples in this Letter. The nanoindentation process was performed through an canonical ensemble NVE (with system of particle number N, volume V, energy E). Furthermore, nanoindentation was performed along z, using a tip at radii of 3.5, 5, and 7 nm. To set up boundary conditions along the depth (d_z), the samples are divided into three sections in the z direction: a frozen section for numerical cell stability ($0.02 \times d_z$), a thermostatic section to dissipate heat from nanoindentation ($0.08 \times d_z$) and a dynamical atoms section where the surface structure is modified by the indenter tip. A 5 nm vacuum section was also included as an open boundary at the top of the sample. The indenter tip is assumed to be a rigid sphere with force: $F(t) = K[\vec{r}(t) - R]^2$, where $K = 1000$ eV/Å^3 and R is the tip radius, moving along the z direction with a speed of $v = 20$ m/s, a value which is independent of the final result of our study. Also, the tip velocity is below the speed of sound in solids [50]. This allows us to capture the elastic Hertzian regime and model early dislocation nucleation [51–53]. The methods are elaborated further in Supplemental Material [54]. In addition, we randomly changed the position of the indenter tip center to ten different locations to account for statistical variability in our results, across three different samples (RSS, SRO, DWO) with all the samples considered with the same box size of $25.85 \times 23.59 \times 15.14$ nm^3. Additionally, to ensure that results are not affected by the underlying atomic structure,

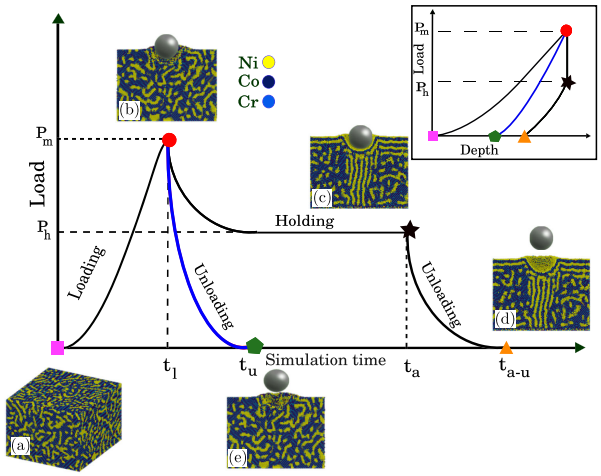

FIG. 1. Nanoindentation protocol for SRO reorganization in equiatomic NiCoCr alloys. The process starts when the aged NiCoCr sample (a) is indented up to a certain depth (b). Afterward, the indenter's velocity is set to zero, this is the moment when the hybrid MD-MC process starts again and leads to a configuration in which Ni and Co-Cr segregate or are no longer randomly distributed but are reorganized and form stripe patterns under the indenter tip (c). The resulting pattern retains its shape even after the indenter is removed from the sample (d). This pattern is not observed during normal loading-unloading nanoindentation simulation like the process shown by the blue line (e). The inset figure displays the corresponding processes in the load-depth coordinates, where symbol types define the loading path.

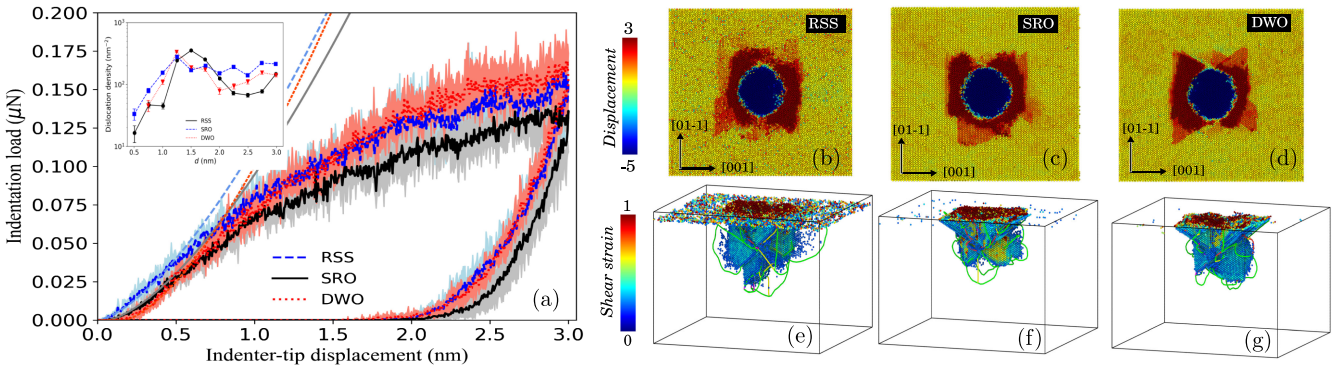

FIG. 2. Nanoindentation-induced reorganization of short-range ordering in metallic alloys. (a) Load-displacement (LD) curves, along with the Hertz fitting, for a random solid solution (RSS), an annealed sample, and a DWO sample created out of the dwell nanoindentation protocol with an indenter of radius 20 nm and in the elastic regime. The annealed and striped samples exhibit higher strength compared to the RSS. The inset shows the effect of sample preparation on dislocation density evolution during the loading process. (b)–(d) Pileup patterns for RSS, annealed (SRO), and striped (DWO) FCC samples preserving the characteristic fourfold symmetry rosette. (e)–(g) Stacking planes identified by a shear-strain mapping and dislocation network underneath the indenter tip, illustrating the smaller plastic region for the annealed and striped samples.

we studied five equiatomic samples for each crystal orientation, differing in their initial RSS atomic positions. As shown in Fig. 1, when the indenter reached the target depth (1, 2, or 3 nm), v was set to zero and then MC thermal relaxation ("holding") process was performed using the variance-constrained semigrand canonical (VCSGC) ensemble [27,61] at $T = 300$ K. The chemical potential differences $\Delta\mu_{\text{Ni-Cr}} = -0.31$ and $\Delta\mu_{\text{Ni-Co}} = 0.021$ and the variance constraint $\kappa = 1000$ are set as in Ref. [27]. The holding part (cf. Fig. 1) includes 1 MC cycle for every 20 MD steps within the VCSGC ensemble for a total number of 150000 MC cycles, ensuring that the thermalized configuration contains stable SRO patterning.

In the studied protocol (cf. Fig. 1), equiatomic NiCoCr, which has been shown to display Ni-rich SRO patterns [27], is indented to a specified indentation depth in the "loading" step. The CSRO changes only during the holding step, where the indenter is held fixed and thermomechanical MC-MD relaxation is performed at room temperature (cf. Fig. 1). Because of holding, a load drop is commonly observed from maximum P_m at time t_l to P_h at time t_a. The "unloading" step consists of removing the load altogether at a velocity of $v = -20$ nm/s, using MD, and then perform further MC-MD relaxation at the sample. We find that a characteristic DWO pattern emerges after unloading at $t_{\text{a-u}}$ (cf. Fig. 1), that would not appear without the holding stage. The whole protocol is also illustrated in the load-depth plot in the inset of Fig. 1.

The characterization of the resulting nanoindentation-driven DWO pattern observed in our simulations, is shown and compared to a RSS and a Ni-rich SRO sample in Fig. 2. The DWO and SRO rich samples happen to have a larger mechanical strength and hardness than a RSS, as their load-depth (P-d) curves illustrate in Fig. 2(a). This could be due to the already observed Ni-dominated solute segregation, that is pinning and obstructing dislocation motion [17,62]. This phenomenon may also be implied by a drastic dislocation density increase for DWO and SRO samples at smaller depths, compared to RSS ones, as shown in the inset of Fig. 2(a). Although the fourfold rosette pileup pattern is preserved for all the samples due to FCC crystal structure [Figs. 2(b)–2(d)], the RSS plastic zone is typically larger than those of the DWO and SRO samples, as shown in Figs. 2(e)–2(g), concluding that SRO and DWO have analogous dislocation pinning effects.

The character and origin of the emergent DWO onset was further investigated, by considering the effect of crystal orientation. We find that the behavior for crystals along $x = [100]$, $y = [010]$, and $z = [001]$ [cf. Fig. 3(b)] is drastically different from the original orientation behavior [cf. Fig. 3(a)] with the DWO orientation being tilted. However, further inspection shows that DWO forms along $z = [011]$ universally in the same direction relative to the crystal [cf. Fig. 3(b)]. The same protocol yields asymmetric outcomes in tension and compression tests, with reorganization evident in tension but not in compression (see Supplemental Material [54]). The DWO pattern also aligns with the maximum von Mises and principal stress, accumulated in the [011] planes [cf. Figs. 3(c) and 3(d)], a fact that implies material anisotropy. To further elucidate this issue, we estimate the pairwise potential energy for the Ni-Ni, Ni-Cr, and Ni-Co pairs in a RSS crystal oriented in $x = [100]$, $y = [01\bar{1}]$, and $z = [011]$, as shown in Fig. 3 [cf. 3(f)], is calculated for each atom [cf. Fig. 3(e)], considering only the first nearest neighbors defined by the first pick of the pair correlation function $g(r)$ (3 Å). With this input, we compare the total energy of a DWO ansatz (see Supplemental Material for details [54]) order that compares well with Fig. 3(a) and contains the interstripe distance as a free parameter. By comparing this

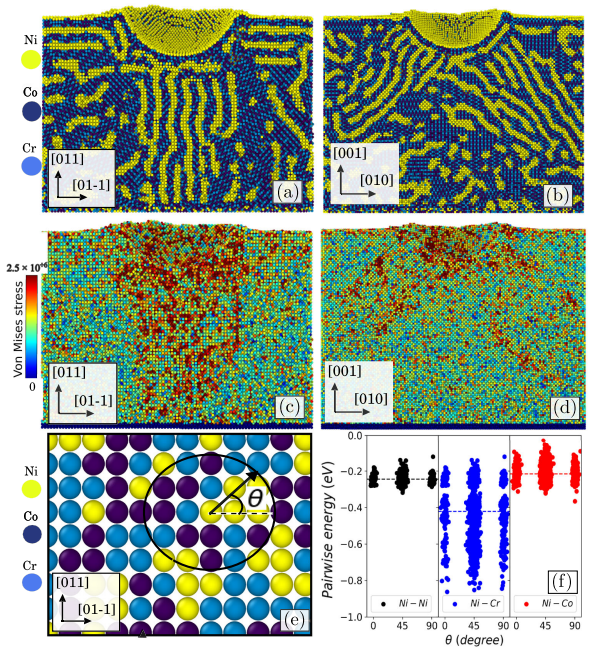

FIG. 3. Origin of nanoindentation-driven reorganization of short-range ordering. (a),(b) are the SRO patterns found along the $z[011]$ and $z[001]$ orientations, respectively. (c),(d) illustrate the correlation between the stripe patterns' orientation shown in (a),(b) and the von Mises stress. The pairwise energy between Ni-Ni, Ni-Cr, and Ni-Co atoms within each atom's neighbor list (e) is plotted in the same plane in (a) (but for separate Ni, Ni-Cr, and Ni-Co crystals) with respect to the in-plane angle of the pair atoms (f). As shown in (f), the Ni-Cr pairs have an average energy lower by 3 orders of magnitude compared to Ni-Ni and Ni-Co pairs.

DWO ansatz energy to the energy of RSS samples, we find that the optimal interstripe distance is very close to the one realized in MD simulations. In this way, we conclude that the DWO emergence is deeply linked to the energetic features of the interatomic potential, which is also the key cause of SRO emergence in equiatomic NiCoCr simulations. These peculiarities are also sufficient to closely resemble the nanometer-scale observations of SRO made possible by advanced experimental tools [9]. In order to verify our results, a comparison with an alternative interatomic potential, developed by Farkas *et al.* [59], is made. In that case, SRO is not observed, neither during aging [17], nor after the nanoindentation protocol implemented in the current work.

The emergent DWO displays strong size effects [63], which are dependent on the indentation depth and indenter tip radius as a function of temperature (cf. Fig. 4). In our displacement-controlled tests, we find that load-time (P-t) curves [cf. Figs. 4(a)–4(c)] display a larger load drop [63] during holding as depth or tip radius increases, leading to spatially extended DWO (cf. Fig. 4), resembling the plastic zone size. While not studied here, we also expect that size-dependent strain bursts should be observed in load-controlled tests. More specifically, the protocol discussed in Fig. 1 is implemented for two different indenter depths (1 and 3 nm) while the temperature (300 K) and the indenter tip radii (3.5 nm) are kept fixed [cf. Figs. 4(d) and 4(e)]. Furthermore, increasing the indenter radii from 2 to 7 nm gives rise to a larger plastic zone and as a result, a larger DWO pattern [cf. Figs. 4(h) and 4(i)]. This effect can also be observed from the larger load drop observed in the P-t curves for the larger radii [cf. Fig. 4(c)]. However, increasing the temperature (from 300 to 400 K), while the indenter depth and radii are the same, also results in a more organized DWO pattern shown in Fig. 4 [cf. 4(f) and 4(g)], but there is no pronounced size effect, as shown by the absence of a load-drop decrease [cf. Fig. 4(b)].

Given the elusive character of SRO formation in advanced alloys [31], the described dynamic nanoindentation protocol appears to be a plausible candidate for nanoscale manipulation and control of CSRO patterns in equiatomic NiCoCr and possibly, other multicomponent alloys. By the investigation of thermomechanical features

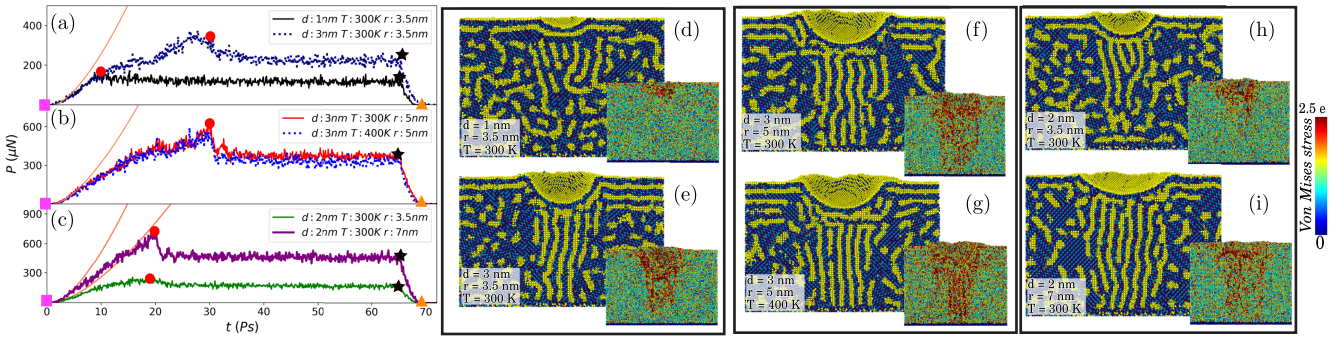

FIG. 4. Effect of size and temperature on nanoindentation-driven reorganization of short-range ordering. Load-redtime (P-t) curves for nanoindentation at different holding depths are shown in (a), where a larger holding depth results in more pronounced stripe patterns as depicted in (d),(e). The corresponding von Mises stress values, in units of gigapascals, are shown in inset snapshots of (d)–(i) and exhibit a similar correlation with the stripe patterns. Increasing the temperature by 100 K in (b) results in a more organized stripe pattern (f),(g) due to higher von Mises stress values (more red spots in the inset). The increase of indenter radius leads into a larger load drop (c) and affects the pattern size, as shown in (h),(i).

and size effects, we conclude that atomic scale Ni-rich segregation strongly influences the mechanical properties of equiatomic NiCoCr, in a way that can be quantified in dynamic nanoindentation. CSRO reorganization mechanisms in NiCoCr are shown to be energetic in character (as opposed to entropic) leading to highly complex and anisotropic patterns in space. Such morphological complexities may not be fully captured by the classical Guinier-Preston (GP) zone model describing early-stage kinetics of precipitation hardening as a transition from RSS states to clustered configurations. More recent approaches aim to incorporate local chemical complexities by considering the dominant role of enthalpic interactions over configurational entropic effects and their influence in short-range ordering [27]. In our study, the origin of DWO emergence is tracked back at the potential energy surface of a RSS crystal. Finally, the pronounced observed size effects of the emergent DWO suggest that, for experimentally relevant nanoindentation depths and tip radii, the emergent DWO shall be visible under common electron microscopy tools at the nanoscale.

As a concluding remark, the emergence of Ni-rich SROs under thermal annealing and their further enhancement due to the stress concentration could be a rather generic feature, not specific to particular chemical compositions and/or simulation details employed in this study. By utilizing a different interatomic potential in binary $Ni_{90}Al_{10}$, $Ni_{76}Al_{24}$, and $Ni_{60}Al_{40}$ alloys [57], we present evidence that the emerging stripelike patterns associated with Ni-based clusters may indeed constitute fairly universal mechanisms that could be understood from basic energetic arguments (see Supplemental Material [54] for further details). Nevertheless, it is necessary to explore the robustness of these findings across a broader range of chemically complex alloys by experimental means.

We would like to thank Mikko Alava, Pawel Sobkowicz, and Lukasz Kurpaska for fruitful discussions on features of short-range order. We acknowledge support from the European Union Horizon 2020 research and innovation program under Grant Agreement No. 857470 and from the European Regional Development Fund via the Foundation for Polish Science International Research Agenda PLUS program Grant No. MAB PLUS/2018/8.

*stefanos.papanikolaou@ncbj.gov.pl

[1] B. Cantor, I. Chang, P. Knight, and A. Vincent, Mater. Sci. Eng. **375–377**, 213 (2004).
[2] J.-W. Yeh, S.-K. Chen, S.-J. Lin, J.-Y. Gan, T.-S. Chin, T.-T. Shun, C.-H. Tsau, and S.-Y. Chang, Adv. Eng. Mater. **6**, 299 (2004).
[3] D. B. Miracle, J. D. Miller, O. N. Senkov, C. Woodward, M. D. Uchic, and J. Tiley, Entropy **16**, 494 (2014).
[4] Z. Li, S. Zhao, R. O. Ritchie, and M. A. Meyers, Prog. Mater. Sci. **102**, 296 (2019).
[5] Y. Shang, J. Brechtl, C. Psitidda, and P. K. Liaw, arXiv: 2102.09055.
[6] B. Gludovatz, A. Hohenwarter, K. V. S. Thurston, H. Bei, Z. Wu, E. P. George, and R. O. Ritchie, Nat. Commun. **7**, 10602 (2016).
[7] Y. Wu, F. Zhang, X. Yuan, H. Huang, X. Wen, Y. Wang, M. Zhang, H. Wu, X. Liu, H. Wang *et al.*, J. Mater. Sci. Technol. **62**, 214 (2021).
[8] L. Zhou, Q. Wang, J. Wang, X. Chen, P. Jiang, H. Zhou, F. Yuan, X. Wu, Z. Cheng, and E. Ma, Acta Mater. **224**, 117490 (2022).
[9] X. Chen, Q. Wang, Z. Cheng, M. Zhu, H. Zhou, P. Jiang, L. Zhou, Q. Xue, F. Yuan, J. Zhu *et al.*, Nature (London) **592**, 712 (2021).
[10] F. Walsh, M. Asta, and R. O. Ritchie, Proc. Natl. Acad. Sci. U.S.A. **118**, e2020540118 (2021).
[11] F. X. Zhang, S. Zhao, K. Jin, H. Xue, G. Velisa, H. Bei, R. Huang, J. Y. P. Ko, D. C. Pagan, J. C. Neuefeind, W. J. Weber, and Y. Zhang, Phys. Rev. Lett. **118**, 205501 (2017).
[12] Y. Ma, G. Peng, D. Wen, and T. Zhang, Mater. Sci. Eng. **621**, 111 (2015).
[13] C. Guo, Y. Fang, F. Chen, and T. Feng, Intermetallics **110**, 106480 (2019).
[14] R. Zhang, S. Zhao, J. Ding, Y. Chong, T. Jia, C. Ophus, M. Asta, R. O. Ritchie, and A. M. Minor, Nature (London) **581**, 283 (2020).
[15] W. He, Q. Zeng, C. Yan, J. Zhu, D. Zhang, and J. Cao, J. Mater. Sci. Technol. **101**, 173 (2022).
[16] Y. Lai, J. Yu, L. Sun, F. Wang, Q. Zheng, and H. He, J. Non-Cryst. Solids **597**, 121906 (2022).
[17] A. H. Naghdi, K. Karimi, A. E. Poisvert, A. Esfandiarpour, R. Alvarez, P. Sobkowicz, M. Alava, and S. Papanikolaou, Phys. Rev. B **107**, 094109 (2023).
[18] B. Yin, S. Yoshida, N. Tsuji, and W. A. Curtin, Nat. Commun. **11**, 2507 (2020).
[19] Q. Ding, Y. Zhang, X. Chen, X. Fu, D. Chen, S. Chen, L. Gu, F. Wei, H. Bei, Y. Gao, M. Wen, J. Li, Z. Zhang, T. Zhu, R. O. Ritchie, and Q. Yu, Nature (London) **574**, 223 (2019).
[20] M. Widom, W. P. Huhn, S. Maiti, and W. Steurer, Metall. Mater. Trans. A **45**, 196 (2014).
[21] A. Tamm, A. Aabloo, M. Klintenberg, M. Stocks, and A. Caro, Acta Mater. **99**, 307 (2015).
[22] L. J. Santodonato, Y. Zhang, M. Feygenson, C. M. Parish, M. C. Gao, R. J. Weber, J. C. Neuefeind, Z. Tang, and P. K. Liaw, Nat. Commun. **6**, 5964 (2015).
[23] P. Singh, A. V. Smirnov, and D. D. Johnson, Phys. Rev. B **91**, 224204 (2015).
[24] L. Koch, F. Granberg, T. Brink, D. Utt, K. Albe, F. Djurabekova, and K. Nordlund, J. Appl. Phys. **122**, 105106 (2017).
[25] A. Fernández-Caballero, J. S. Wróbel, P. M. Mummery, and D. Nguyen-Manh, J. Phase Equilib. Diffus. **38**, 391 (2017).
[26] Y. Ma, Q. Wang, C. Li, L. J. Santodonato, M. Feygenson, C. Dong, and P. K. Liaw, Scr. Mater. **144**, 64 (2018).
[27] Q.-J. Li, H. Sheng, and E. Ma, Nat. Commun. **10**, 3563 (2019).
[28] H. S. Oh, S. J. Kim, K. Odbadrakh, W. H. Ryu, K. N. Yoon, S. Mu, F. Körmann, Y. Ikeda, C. C. Tasan, D. Raabe, T. Egami, and E. S. Park, Nat. Commun. **10**, 2090 (2019).

[29] W.-R. Jian, Z. Xie, S. Xu, Y. Su, X. Yao, and I. J. Beyerlein, Acta Mater. **199**, 352 (2020).
[30] J. B. Seol, W.-S. Ko, S. S. Sohn, M. Y. Na, H. J. Chang, Y.-U. Heo, J. G. Kim, H. Sung, Z. Li, E. Pereloma *et al.*, Nat. Commun. **13**, 6766 (2022).
[31] E. George, W. Curtin, and C. Tasan, Acta Mater. **188**, 435 (2020).
[32] J. Ding, Q. Yu, M. Asta, and R. O. Ritchie, Proc. Natl. Acad. Sci. U.S.A. **115**, 8919 (2018).
[33] M. Lenz, Y. M. Eggeler, J. G. Müller, C. H. Zenk, N. Volz, P. Wollgramm, G. Eggeler, S. Neumeier, M. Göken, and E. Spiecker, Acta Mater. **166**, 597 (2019).
[34] A. Bezold, N. Volz, F. Xue, C. H. Zenk, S. Neumeier, and M. Göken, Metall. Mater. Trans. A **51**, 1567 (2020).
[35] F. Xue, C. Zenk, L. Freund, M. Hoelzel, S. Neumeier, and M. Göken, Scr. Mater. **142**, 129 (2018).
[36] C. H. Zenk, N. Volz, C. Zenk, P. J. Felfer, and S. Neumeier, Crystals **10**, 1058 (2020).
[37] R. K. Rhein, P. G. Callahan, S. P. Murray, J.-C. Stinville, M. S. Titus, A. Van der Ven, and T. M. Pollock, Metall. Mater. Trans. A **49**, 4090 (2018).
[38] L. Feng, D. Lv, R. Rhein, J. Goiri, M. Titus, A. Van der Ven, T. Pollock, and Y. Wang, Acta Mater. **161**, 99 (2018).
[39] J. May, H. Höppel, and M. Göken, Scr. Mater. **53**, 189 (2005).
[40] N. Chinh, P. Szommer, Z. Horita, and T. Langdon, Adv. Mater. **18**, 34 (2006).
[41] Y. Li, J. Mueller, H. Höppel, M. Göken, and W. Blum, Acta Mater. **55**, 5708 (2007).
[42] Q. Wei, S. Cheng, K. Ramesh, and E. Ma, Mater. Sci. Eng. **381**, 71 (2004).
[43] H. Höppel, J. May, and M. Göken, Adv. Eng. Mater. **6**, 781 (2004).
[44] V. Maier, B. Merle, M. Göken, and K. Durst, J. Mater. Res. **28**, 1177 (2013).
[45] W. H. Poisl, W. C. Oliver, and B. D. Fabes, J. Mater. Res. **10**, 2024 (1995).
[46] B. N. Lucas and W. C. Oliver, Metall. Mater. Trans. A **30**, 601 (1999).
[47] D. S. Stone, J. E. Joseph, J. Puthoff, and A. A. Elmustafa, J. Mater. Res. **25**, 611 (2010).
[48] I.-C. Choi, B.-G. Yoo, Y.-J. Kim, and J.-i. Jang, J. Mater. Res. **27**, 3 (2012).
[49] A. P. Thompson, H. M. Aktulga, R. Berger, D. S. Bolintineanu, W. M. Brown, P. S. Crozier, P. J. in 't Veld, A. Kohlmeyer, S. G. Moore, T. D. Nguyen, R. Shan, M. J. Stevens, J. Tranchida, C. Trott, and S. J. Plimpton, Comput. Phys. Commun. **271**, 108171 (2022).
[50] J. Varillas, J. Očenášek, J. Torner, and J. Alcalá, Acta Mater. **217**, 117122 (2021).
[51] F. Domínguez-Gutiérrez, S. Papanikolaou, A. Esfandiarpour, P. Sobkowicz, and M. Alava, Mater. Sci. Eng. **826**, 141912 (2021).
[52] L. Kurpaska, F. Dominguez-Gutierrez, Y. Zhang, K. Mulewska, H. Bei, W. Weber, A. Kosinka, W. Chrominski, I. Jozwik, R. Alvarez-Donado, S. Papanikolaou, J. Jagielski, and M. Alava, Mater. Des. **217**, 110639 (2022).
[53] F. J. Domínguez-Gutiérrez, P. Grigorev, A. Naghdi, J. Byggmästar, G. Y. Wei, T. D. Swinburne, S. Papanikolaou, and M. J. Alava, Phys. Rev. Mater. **7**, 043603 (2023).
[54] See Supplemental Material at http://link.aps.org/supplemental/10.1103/PhysRevLett.132.116101 for more details on the methods, deeper analysis of the results, and more simulation examples, including Refs. [17,30,50–52,55–60].
[55] A. Stukowski, Model. Simul. Mater. Sci. Eng. **18**, 015012 (2010).
[56] S. Picak, J. Liu, C. Hayrettin, W. Nasim, D. Canadinc, K. Xie, Y. Chumlyakov, I. Kireeva, and I. Karaman, Acta Mater. **181**, 555 (2019).
[57] A. Abu-Odeh and M. Asta, Acta Mater. **226**, 117615 (2022).
[58] C. Wolverton, V. Ozolins, and A. Zunger, J. Phys. Condens. Matter **12**, 2749 (2000).
[59] D. Farkas and A. Caro, J. Mater. Res. **33**, 3218 (2018).
[60] W. Huang and Y. Chang, Intermetallics **6**, 487 (1998).
[61] B. Sadigh, P. Erhart, A. Stukowski, A. Caro, E. Martinez, and L. Zepeda-Ruiz, Phys. Rev. B **85**, 184203 (2012).
[62] A. Esfandiarpour, S. Papanikolaou, and M. Alava, Phys. Rev. Res. **4**, L022043 (2022).
[63] S. Papanikolaou, Y. Cui, and N. Ghoniem, Model. Simul. Mater. Sci. Eng. **26**, 013001 (2017).